LOAN DOCUMENT

PHOTOGRAPH THIS SHEET

DTIC ACCESSION NUMBER

LEVEL

INVENTORY 0

Model-Based Data Fusion and Discrimination - - - - -

DOCUMENT IDENTIFICATION

25 Dec 98

DISTRIBUTION STATEMENT A
Approved for Public Release
Distribution Unlimited

DISTRIBUTION STATEMENT

HANDLE WITH CARE

ACCESSION FOR
NTIS GRA&I ☐
DTIC TRAC ☐
UNANNOUNCED ☐
JUSTIFICATION

BY

DISTRIBUTION/

AVAILABILITY CODES

DISTRIBUTION	AVAILABILITY AND/OR SPECIAL	
A-1		

DISTRIBUTION STAMP

DATE ACCESSIONED

DATE RETURNED

DTIC QUALITY INSPECTED 4

20000720 093

DATE RECEIVED IN DTIC

REGISTERED OR CERTIFIED NUMBER

PHOTOGRAPH THIS SHEET AND RETURN TO DTIC-FDAC

DTIC FORM 70A JUN 90

DOCUMENT PROCESSING SHEET

PREVIOUS EDITIONS MAY BE USED UNTIL STOCK IS EXHAUSTED.

LOAN DOCUMENT

MODEL-BASED DATA FUSION AND DISCRIMINATION OF UXO IN MAGNETOMETRY AND EM SURVEYS

SERDP Project CU/1092/8

ANNUAL REPORT - FY 1998

12/25/98

J.R. McDonald
Naval Research Laboratory
Washington, DC

Robert Grimm
Blackhawk Geometrics
Golden, CO

REPORT DOCUMENTATION PAGE

Form Approved
OMB No. 074-0188

1. AGENCY USE ONLY (Leave blank)	2. REPORT DATE	3. REPORT TYPE AND DATES COVERED
	December 25, 1998	Annual Report – FY 1998

4. TITLE AND SUBTITLE
Model-Based Data Fusion and Discrimination of UXO in Magnetometry and EM Surveys

5. FUNDING NUMBERS
N/A

6. AUTHOR(S)
J.R. McDonald and Robert Grimm

7. PERFORMING ORGANIZATION NAME(S) AND ADDRESS(ES)
Naval Research Laboratory, Washington DC
Blackhawk Geometrics, Golden, CO

8. PERFORMING ORGANIZATION REPORT NUMBER
N/A

9. SPONSORING / MONITORING AGENCY NAME(S) AND ADDRESS(ES)
SERDP
901 North Stuart St. Suite 303
Arlington, VA 22203

10. SPONSORING / MONITORING AGENCY REPORT NUMBER
N/A

11. SUPPLEMENTARY NOTES

12a. DISTRIBUTION / AVAILABILITY STATEMENT
Approved for public release: distribution is unlimited.

12b. DISTRIBUTION CODE
A

13. ABSTRACT ***(Maximum 200 Words)***

Locating, identifying and disposing of buried UXO on the 10 million acres of contaminated lands in the continental United States is a 500 billion dollar problem. Development of new technologies with improved data analysis has been identified as a high priority triservice requirement. Using current methods, it has been shown that false alarm detections far outnumber correctly identified ordnance. The best performing technologies typically have a false alarm rate of 300-500%. The high cost of digging and siposing of targets accounts for the overwhelming portion of the costs of UXO remediation, therefore a substantial saving could be recognized if the number of false positives were reduced. Using data collected by the Naval Research Laboratory's MTADS, new software techniques are being developed to improve discrimination and reduce the false alarm rate.

14. SUBJECT TERMS	15. NUMBER OF PAGES
SERDP, SERDP Collection, UXO, magnetrometry, ordnance	34
	16. PRICE CODE N/A

17. SECURITY CLASSIFICATION OF REPORT	18. SECURITY CLASSIFICATION OF THIS PAGE	19. SECURITY CLASSIFICATION OF ABSTRACT	20. LIMITATION OF ABSTRACT
unclass	unclass	unclass	UL

CONTENTS

FIGURES

SERDP ANNUAL REPORT - FY 1998
(Project CU/1092/8)
12/25/98

1. PROJECT TITLE

Model-Based Data Fusion and Discrimination of UXO in Magnetometry and EM Surveys

2. PERFORMING ORGANIZATION

LEAD ORGANIZATION

Naval Research Laboratory - Washington, D.C.
PI: Dr. Jim McDonald

PARTNERING ORGANIZATION

Blackhawk Geometrics
P.I. Dr. Robert Grimm

3. PROJECT BACKGROUND

Locating, identifying and disposing of buried UXO on the 10 million acres of contaminated lands in the continental United States is a 500 billion dollar problem. Development of new technologies with improved data analysis has been identified as a high priority triservice requirement. Using current methods, it has been shown that false alarm detections far outnumber correctly identified ordnance. The best performing technologies typically have a false alarm rate of 300-500%.[2-5] The high cost of digging and disposing of targets accounts for the overwhelming portion of the costs of UXO remediation, therefore a substantial saving could be recognized if the number of false positives were reduced. Using data collected by the Naval Research Laboratory's *MTADS*, new software techniques are being developed to improve discrimination and reduce the false alarm rate. The program has three parts: Phase 1, Target Detection, Phase 2, Quantitative Modeling, and Phase 3, Target Classification.

4. PROJECT OBJECTIVE

The objective of this project is the development of new data analysis methods for the best available sensor suites. Data fusion and classifier techniques will be used to better allow discrimination between intact ordnance and the typical clutter associated with target and bombing ranges. Improved physical modeling, (to better represent three-dimensional shapes rather than models based on point dipoles) will be developed. Specifically, NRL will develop software techniques to allow discrimination of intact ordnance from Ordnance Explosive Wastes (OEW) using arrays of full-field magnetometers and time-domain electromagnetic sensors as the primary detection tools. These goals will be accomplished by developing new methods for target identification, physical modeling, and probabilistic classification that uses the sensor data sets jointly. NRL's Multi-Sensor Towed Array Detector System (*MTADS*) will be the primary platform for which the software will be designed, although the work is applicable to any magnetic and EM array measurements and some aspects of the development are relevant to other types of sensor data.

5. TECHNICAL APPROACH AND RISKS

The key goals of UXO classification and OEW discrimination can best be achieved by a thorough consideration of the fundamental physics of sensors and a development of classification schemes, based on physical understanding, that provide quantitative confidence levels. Therefore, we favor an approach that is model-based rather than one based upon the use of raw data. The latter approach performs classification directly from sensor data, whereas this approach performs a joint transform of data to derive physical parameters (position, depth, orientation) allowing the classification to be based primarily on shape information and the intrinsic variables. However, to improve the efficiency with which analyses can be carried out, we are adopting a threefold approach. Initially, raw magnetometry and EM survey data that have been preprocessed (to integrate navigation and sensor data) and mapped onto a two dimensional grid that can be automatically processed using principal component analysis to isolate targets with common features in the multiple data sets. Based upon initial studies with *MTADS* data from Twentynine Palms and the Badlands Bombing Range, we expect that using this data based approach, 70-90% of targets can be automatically selected and analyzed. Following the automatic target selection process, we use the model-based quantitative magnetic and EM routines to solve the inverse problem for target position, depth, shape, and orientation. Then a probabilistic classifier (Bayesian or neural net) will be trained to discriminate UXO from OEW and other clutter. The resulting model will identify likely UXO in the presence of other clutter. Finally, the system will be interactive to allow an analyst, (as a backup to the automatic target picker) to review individual graphical images and to pick additional targets. The latter analysis will document those targets that are too deep to be seen by the EM array, and shallow targets that are too small to be identified by the magnetometer array. All three tasks involve novel methods not in use by others. The output of the output of the target analysis process is a target list with probabilities associated with each target predicting the likelihood that is intact ordnance.

6. PROJECT ACCOMPLISHMENTS

6.1 TARGET DETECTION

Target Detection is focused on automation and inclusion of all available data. Manual target detection is time-consuming, requires an expert operator, and is difficult to consider more than one channel of data at a time. Experts screen the magnetometer data and select potential UXO targets based on experience and intuition. Little use of the EM data is involved in the initial steps of this process. Ideally, the target detection step will use the all the data available, and since this program will have a separate classifier step, the automated target detection method need not include UXO classification. Subsequently, target identification, assignment of associated confidence levels, and classification will be done by the modeling and classification algorithms being developed in Phases 2 and 3 of this program. The goal of this program is to have the modeler-classifier operate on the maximum reasonable number of targets because computational power is not limited. Digital filtering and PCA methods are being developed to pre-process the data prior to automated anomaly picking. Digital filtering is being used to enhance important features and reduce noise, while principal component analysis is being used to fuse three channels of data and reduce noise. Automated methods have been developed to pick targets. For this

program, the fundamental requirement for a successful automatic anomaly picker is that Type I error (missed detections) must be minimized, even if this means greater Type II error (selection of clutter for the modeler). The anomaly picker is designed such that minimal classification is imposed.

Target detection efforts for this program have used data collected by the *MTADS* at two sites: Badlands Bombing Range in South Dakota[6] and NRL's new ordnance signature test facility at the Army Research Lab in Blossom Point, MD. A wide variety of objects of different shapes, sizes and orientations are buried on the site. In addition, many items of ordnance wastes and scrap removed from previous survey sites have been characterized and buried on site. Finally, a range of inert (intact) ordnance sizes are also contained on the site. There are one and two meter pits on site that have been used to screen the ordnance and shape objects following degaussing. Individual signatures are recorded for each of these objects in a variety of orientations and at various depths. Because this information will be used for evaluation and refinement of fitting algorithms, the buried objects are placed at depths that provide good signal-to-noise signatures for both magnetometer and EM arrays. The Prove Out site is shown in **Figure 1.**

Three data sets, one Mag and Two EM (in orthogonal directions), are being taken for all objects. The data are processed using the baseline *MTADS* DAS, written in IDL 4 (Research System Inc., Boulder, CO) and run on a Silicon Graphics Workstation. These data are available for use in both SERDP and ESTCP programs and will be made available to other developers.

In this program development of PCA methods are being carried out using a Windows 95 version of IDL 5 on a PC. Gaussian filters and multiway PCA methods are being developed using MATLAB (The Math Works, Inc., Natick, MA). In this work, magnetometer and EM survey data are projected onto an x, y grid and the intensity of the signal are displayed in an image. An example of a site is shown in **Figure 2**. Seven 50 meter square data sets or subsets of the sites were used for method development. The Fourier and wavelet filters and the automated anomaly picker were tested on the entire Badlands site using the *MTADS* DAS. Results of these studies were compared to manually generated dig sheets and the remediation results. The three-fold approach to target detection used here involves digital filtering, data fusion, and anomaly picking.

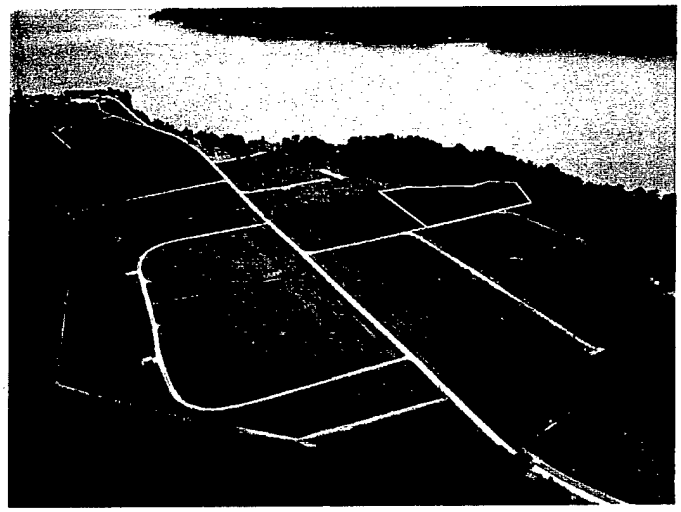

Figure 1. Aerial photograph of the Army Research Lab Facility at Blossom Point, MD. The *MTADS* Prove Out Test Field is in the area shown outlined in yellow.

6.1.1 Digital Filters

We are evaluating the use of digital filtering methods in conjunction with image processing to suppress noise

and enhance the spatial features of interest. As applied to image processing, digital filtering is a neighborhood operation and in this work consists of a two dimensional window that is passed across the image pixel by pixel. The pixels in the windowed region are convoluted with the filter function specified by the user. The product is a new value for the pixel in the center of the window. This type of filtering is sometimes referred to as a sliding neighborhood operation.[7] These methods are particularly valuable to automated *MTADS* data processing when only one channel of data is available and the use of PCA is not possible. The key to using this type of digital filtering is choosing the appropriate filter function. Several different methods were investigated.

Gaussian Filters

Gaussian and Laplacian of Gaussian (LoG) filters were investigated using the MATLAB filtering found in the Image Processing Toolbox[7]. For both types of filters, various widths and window sizes were studied to characterize the performance of the filters on *MTADS* images. MTADS data from the Prove Out and Badlands Sites were used to examine these methods. The routine *fspecial* allows the user to easily compute Gaussian and LoG filters of various widths and windows sizes. Once a filter function is defined, an image can be filtered using the *filter2* routine.

Gaussian and LoG filter were studied using sizes ranging from 5 to 50 and widths ranging from 3 to 20. Several trends were observed. Filtered images obtained using small widths and window sizes looked similar to the raw unfiltered images, while really large widths and window sizes completely suppressed the UXO signatures. In these initial investigations, widths of 10 and a window size of 25 appeared to be a good compromise. **Figure 2** shows the scaled unfiltered image plots of Mag, EM1, and EM2 from the Badlands Site and the filtered images. The Mag image data was obtained using a LoG filter, while EM images were created using Gaussian filters. Comparing the filtered images with the unfiltered images, it is easy to see that filtering does enhance some of the smaller UXO signals. Keeping in mind that the linear filters used in these preliminary studies are quite primitive, better filters tuned to the UXO signatures should provide an even greater enhancement of the signal. The edge effects in the filtered images are an artifact of the linear filtering scheme used in this work and can be eliminated during the filtering process.

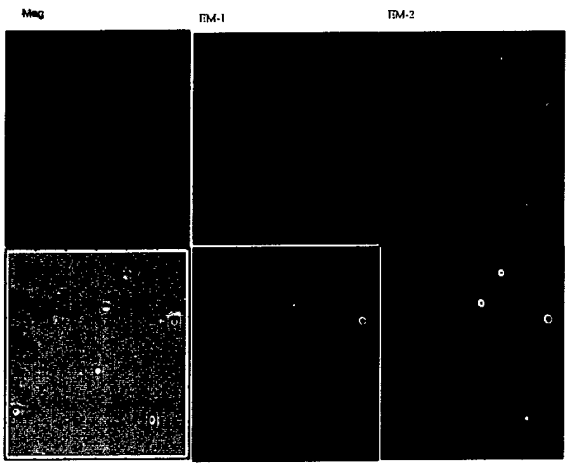

Figure 2. Raw and Filtered images from Badlands Bombing Range. The filtered images on the bottom provide enhanced features and reduced background noise. LoG filter used for Mag data, while Gaussian used for EM surveys.

Fourier Filters

Fourier filtering is well established in data and image processing.[8] A simple 2D band-pass technique, in which the amplitude filter is specified by minimum and maximum spatial frequencies and by a filter ramp coefficient are used here. The filter ramp controls the smoothness of the output image: when set to zero, the minimum and maximum frequencies are the

boundaries of a boxcar-frequency filter and the resulting output image shows some spatial ringing. As the filter ramp is increased, cosine tapers are applied to the edges of the boxcar, and the filter shape approaches a Hanning window, which results in a smoother output image. The specified frequency range always applies to the center of the filter ramp. When combined with linear detrending applied to the whole image, Fourier filtering allows both small-scale noise and large-scale geological background to be rejected in favor of anomalies with spatial scales characteristic of UXO as shown in **Figure 3**.

Wavelet Filters

Wavelets are more recent development that are finding applications in signal processing.[9] Although both the Fourier and wavelet transforms return the same amount of information from a signal of length N, there are different trade-offs between spatial and spectral content. The Fourier transform densely samples the transform domain at spatial frequencies 1/L, 2/L, 3/L, ... where L is the physical length of the data. However, the sine and cosine basis functions of the Fourier transform are globally supported and do not spatially differentiate the signal. In contrast, the wavelet transform encodes spatial variations of scale length, but operates at fewer discrete frequencies 1/L, 2/L, 4/L.... For a 1024-sample signal, then there are 512 Fourier frequencies but only 9 wavelet scales. The choice of the actual length of the wavelet operator (often 4, 12, or 20 samples) determines the trade-off between spatial resolution and smoothness. Wavelets have found strong application in data compression: by choosing a discrete or ramped ("soft") cutoff in transform-coefficient magnitude, often 90% or more of the smallest coefficients can be eliminated and still retain the essential features of an image. In filtering, however, selection of features of interest, such as UXO-scale anomalies, and not the essential features of the image as a whole, which could contain significant non-UXO anomalies are desired.

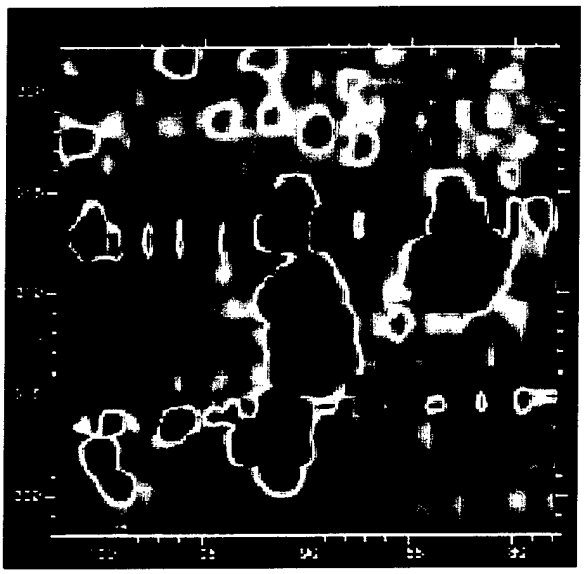

Figure 3a. "Raw" image of EM data, 20-m square, from Badlands Bombing Range (BBR), full-scale range -20 to +50 mV. Large anomalies are displayed in saturation to accentuate small-scale noise and vehicle chatter.

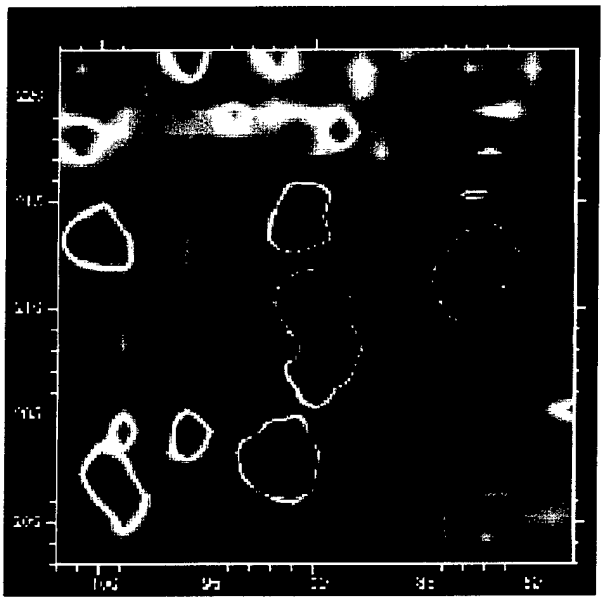

Figure 3b. Fourier-filtered version of image (lowpass wavelengths of 2 m and longer—i.e., frequency less than 0.5 1/m—filter ramp 0.4 1/m).

Hence it was found that coefficient thresholding using Daubechies wavelets was not very useful in the images tested. Therefore bandpass filters similar to those used in Fourier transforms were implemented. Whereas the dense frequency sampling by the Fourier transform allows the 2D frequency-domain filter to be approximately represented as an annulus, the more limited number of spatial scales in the wavelet forces this filter to look like a rotated "L". As shown in **Figure 4**, the output signal from the wavelet bandpass looks squarish because wavelengths at arbitrary azimuths cannot be smoothly represented (the coordinate-axis directions are effectively oversampled), and because the Daubechies wavelets themselves are asymmetric in 2D. It appears that the utility of wavelet filters for UXO is limited, although further tests using smooth, zimuthally symmetric "halo" wavelets might yield better results.

Figure 4. Wavelet-filtered version of Fig. 3 (Daubechies-4 wavelet, lowpass length scales 4 m and longer). Standard wavelets, while well suited to finding the most important features of a scene (image compression), give discretized and squarish outlines as filters.

Principal Component Analyses

Multiway principal component analysis (mPCA) and PCA are the two methods investigated for data fusion of the three data channels. One goal of this research was to test PCA and the recently developed multiway principal component analysis (transform) algorithm, mPCA (or mPCT) for their ability to fuse the individual images from the *MTADS*. It was hypothesized that the mPCA approach would provide better correlation between the images because the horizontal and vertical components of the images are treated separately.

Conventional PCA analysis of multivariate images is a well-understood methodology and is commonly used to process hyperspectral imagery data[10]. Each principal component, A, that is computed attempts to extract correlation (or variation) among the images. In terms of image analysis, the three *MTADS* images (Mag, EM-1, and EM-2) constitute a 3-dimensional matrix, M × N × Q, where M is the number of horizontal pixels (rows), N is the number of vertical pixels (columns), and Q is the number of images or sensors (in this *MTADS* example, Q = 3). It is assumed that the pixels at each x, y address in the three images refer to the same spatial location, otherwise fusion is not possible. The images are unfolded to a produce a two-dimensional matrix (M × N) × Q. Mathematically, the PCA algorithm can be written as

$$X = T \times P + E \qquad (1)$$

where X is the unfolded image matrix, T is an (M×N)×A matrix of PC scores, P is an A × Q matrix of loadings or weights, and E is a matrix of residuals (variations or correlations not explained by

the PCA model). Each column in T can be refolded back to image format to produce a PC scores image (M × N). The loadings for each PC are useful for interpretation.

While the PCA-image processing methodology is well understood, the unfolding and refolding processes cause a loss of spatial information. The rows in the X matrix could be randomly scrambled and the same loadings and scores would be computed. In attempt to regain the spatial information, the mPCA was tested. One of the primary differences between PCA and mPCA is how the data is organized. In mPCA the images are reorganized to a Q × (M × N) matrix. Rather than decompose the data using singular value decomposition (SVD), the mPCA algorithm uses a trilinear decomposition. This approach uses separate SVD calculations for pixels in the horizontal and vertical directions. Mathematically, the mPCA image analysis can be written as

$$X = T \times P_x \times P_y + E \qquad (2)$$

where X is the reorganized image matrix, T is a Q×A matrix of PC scores, P_x is a M × A matrix of loadings or weights, P_y is a N × A matrix of loadings or weights, and E is a matrix of residuals. To produce an image, the kronecker tensor product (') of P_x and P_y is computed and unfolded.[11]

MTADS images from the Prove Out and Badlands sites were evaluated using the mPCA algorithm adapted for multivariate image analysis (*imagempca.m*) and coded in MATLAB. The protocol discussed above for reorganizing the data for the mPCA algorithm was used to pass the images to the *imagempca* routine. The resulting loading vectors (horizontal and vertical) were studied for the first PC. In both data sets, the first PC explained a majority of the variation in the images and no further components were computed. The loading vectors were then recombined to produced a fused image. **Figure 5** shows a fused image from the Prove Out site. It is clear from this image that the mPCA algorithm is not useful for image processing. Unlike the types of data in which the routine was designed, images cannot be written as linear combinations of the horizontal and vertical pixels. This assumption is valid for many applications of mPCA such as chemical sensor systems where the loadings refer to spectral (or sensor) and chromatographic profiles[12]. In image processing, the pixels in the horizontal and vertical directions have the same meaning, thus splitting them apart destroys the majority of the spatial information they contain. Based on these preliminary results no further experiments were conducted in this direction.

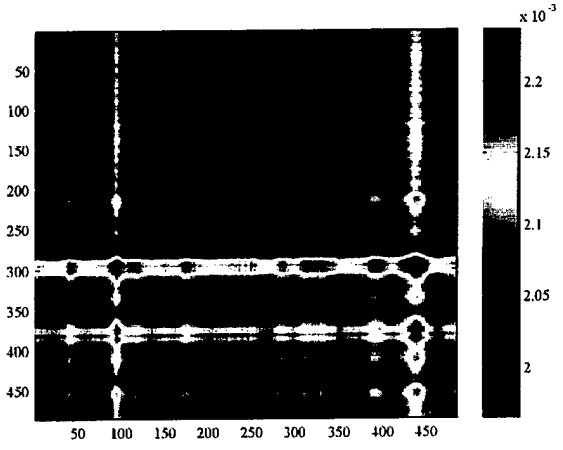

Figure 5. Results of the mPCA study displaying the image of Prove Out Site data set.

Using the pcomp function in IDL 5, PCA of magnetometer and EM data sets from the Prove Out Site were investigated. Examination of the image from the first principal component reveals features from each data set. This confirms the merger of the three channels of data into one image. Using the data sets from the Badlands site and Blossom

Point sites, four variations in the analysis methods have been investigated. Sample covariance and sample correlation matrices were used with and without standardization. Standardizing the variables essentially makes them all 'equally important' by creating new variables with a mean of zero and variance of one. Standardization is important for these data sets since the magnitude of magnetometer and EM

responses are significantly different. PCA using sample covariance and sample correlation matrices both with standardization are equivalent. Inspection of the first-principal component suggests that data fusion of the magnetometer and EM data ha beens accomplished. The new image, which consists of circular features of varying diameters and intensities, reveals features from all three data channels. Data with strong magnetometer and EM signals have the greatest intensity. In most cases, the targets present in the PCA image contained all the targets detected manually for both the Mag and EM data sets. In Badlands Image 1, a "dry hole" that was identified in the Mag image **Figure 6a** is not present in the PCA image as shown in **Figure 6b**. In the Blossom Point Site, several small non-ordnance objects were not present in the PCA image that was detected in the EM image. These objects were small bits of wire and bottle caps. The most important omission in the PCA image was observed in Badlands Image 3. In this case, an M38 bomb and Scrap present in the original Mag image was not present in the PCA image. Inspection of the EM images revealed that it was not present in those images either. Two EM images are used in the PCA application described here while only one Mag image is available. The EM results may be too heavily weighted for some types of data.

The goal was to fuse the data sets equally and not have one type of data be more significant than another at this phase of the analysis. Therefore studies were conducted to optimize the use of the PCA methods. Experiments were designed to investigate how the variations in the data suites influence the results. Four approaches were used. In the first method, the above approach was used where all three data channels, Mag data plus both EM suites are combined in one PCA. The second method used only two channels of data, Mag plus EM1 for the PCA. In the third approach, first principal component was generated from four channels of data, Mag added twice plus both EM data suites. The fourth approach calculated the first principal component for only the two EM surveys, then combined that image with the Mag survey, and performed PCA again. All of the Badlands data sets as well as the Blossom Point data were evaluated in this study and the performance of the methods was compared with the dig sheets manually produced and the actual remediation results. The results of the study vary depending on the data set used. In some cases, there is no difference between the approaches. Doubling the Mag signals was a poor choice due to numerical instabilities, which sometimes caused the system to crash. For the Blossom Point Site, all the PCA methods images that did not contain very small nonordnance targets, small bits of wire and caps. The PCA method that combined Mag with the first principal component of the two EM channels produced an image similar to Mag plus the first EM channel, expect the new image contained less noise. The same results were observed with the Badlands Image 4. The Badlands Image 3 provides the best evidence that the PCA method can be influenced by two EM channels as shown in **Figure 7**. All the approaches that contained an equal number of Mag data channels as EM reveal two targets, a M38 and Scrap, that are present in Mag while not present in the EM surveys. In addition, the fourth approach combining PCA of Mag data with the first principal component of the EM surveys provides a clearer image with less background noise, also shown in **Figure 7**.

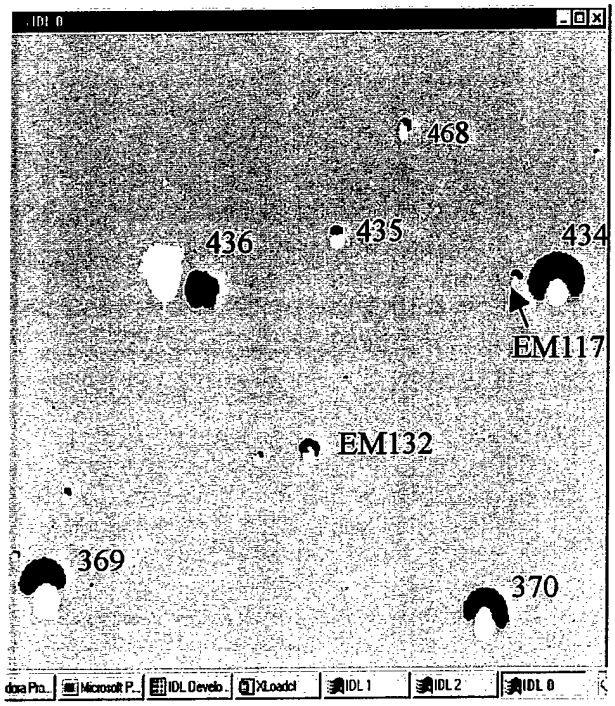

Figure 6a. Badlands Image 1. Dry Hole (target 436) shown in the Mag image.

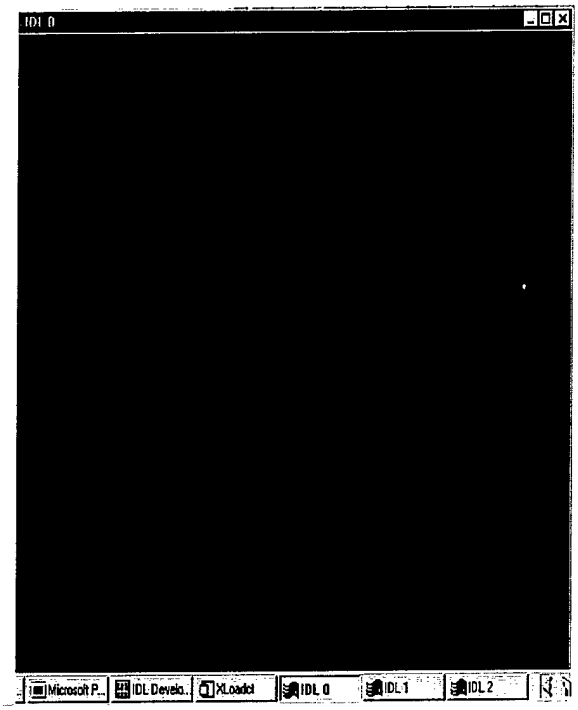

Figure 6b. Badlands Image 1. Dry Hole (target 436) shown in the Mag image (a) is not present in PCA image (b).

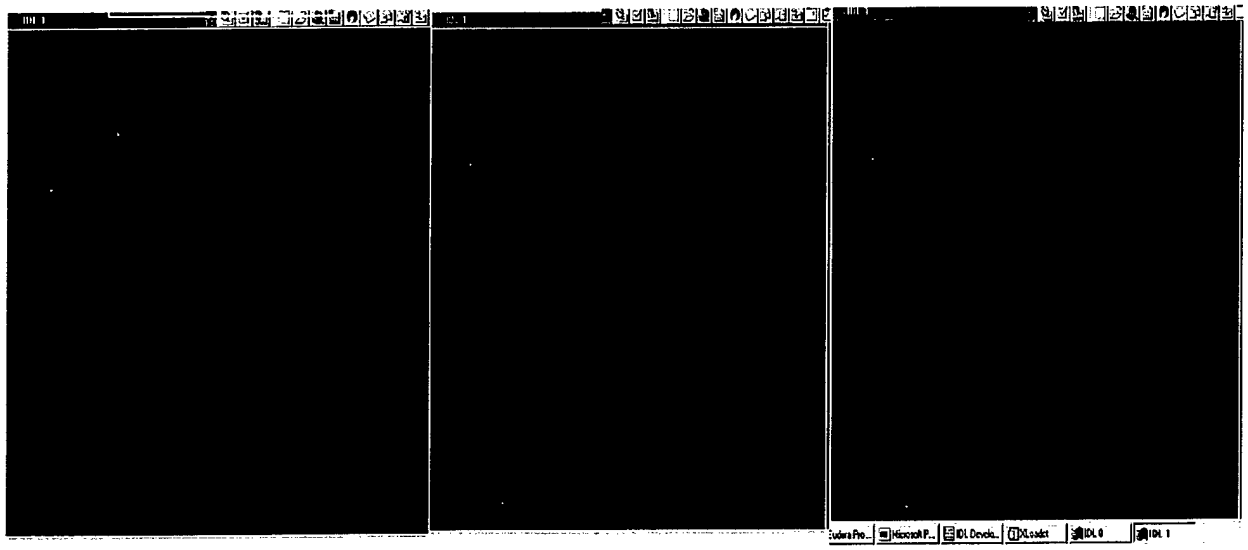

Figure 7. Badlands Image 3. a) PCA of all three channels has two targets missing. b) PCA of Mag and EM1 has targets present. c) The targets are present plus the noise is reduced when PCA is done in two steps, first on the two EM surveys, then on the first principal component of both EM surveys and the Mag data.

PCA was also applied to filtered data. Enhanced features are evident as shown in **Figure 8**. **Figure 8a** shows a PCA scores plot of the raw image from Badlands Image 1, while **Figure 8b** shows a PCA scores plot of the same filtered image. It is clear from these plots that a combination of filtering and PCA can be beneficial for this application.

a) Raw

b) Filtered

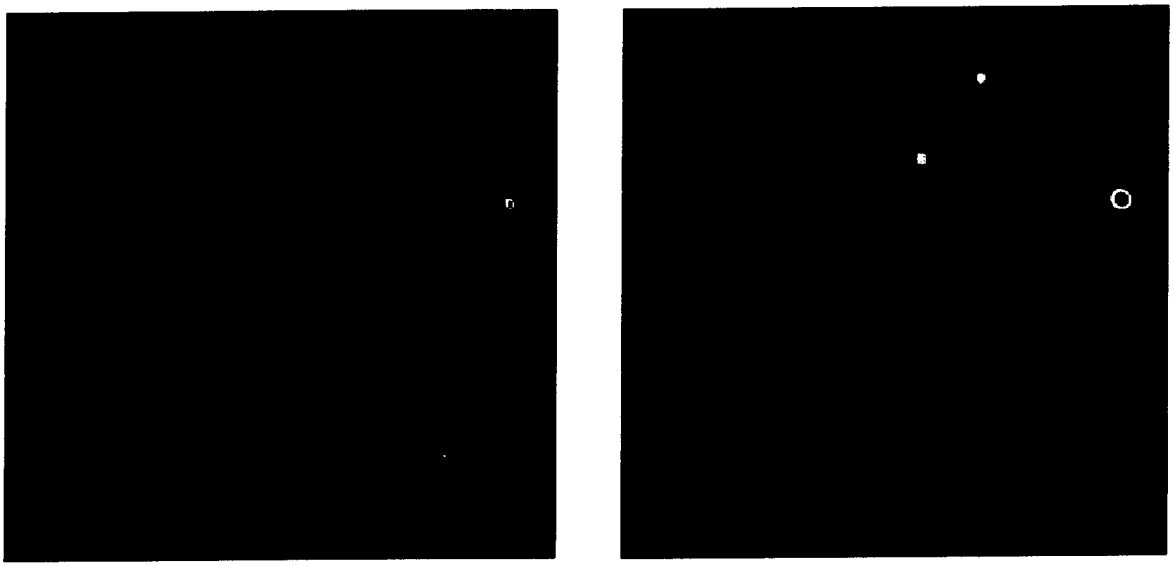

Figure 8. An example of PCA images for both raw (a) and filtered (b) data. In this Badlands image enhanced features are clearly observed for the filtered data.

6.1.2 Anomaly Pickers

The fundamental requirement for a successful automatic anomaly picker is that Type I error (missed detections) must be minimized, even if this means greater Type II error (selection of clutter for the modeler). The anomaly picker is being designed such that minimal classification is imposed, although defining reasonable targets requires development of a selection criterion. The criteria will determine the target size for transport to the modeler. The anomaly picker also provides a user option where the exact parameters (threshold values) are determined interactively by the analyst.

Highlighting anomalies automatically in *MTADS* data is now possible with a tool called the autopicker, which uses parameters selected by the user and a set of rules to draw outlines around anomalies. The full outline of an anomaly is more useful than a peak position or a circular approximation because it contains only the data that is needed by the modeler, reducing computation time and error. EM anomalies are traced differently than magnetic anomalies. EM fitting is treated first. In the first step, the autopicker uses a minimum threshold set by the user to

select anomalies and anomaly groups. For an anomaly standing alone, the outer edge is determined by using a percentage of the peak value, providing the most efficient anomaly shape to the modeler. If anomalies are near enough to each other that the threshold operation groups them together, an uphill-walk algorithm isolates them. Every point in the group anomaly is the starting point for an uphill walk, following the steepest gradient until a peak is reached. The starting point is now associated with that peak and becomes part of a distinct anomaly. An example is shown in **Figure 9**. Groups of peaks are nearly always separable by this method.

Picking magnetic anomalies requires additional steps due to the bimodal nature of the responses. The Mag responses have positive and negative lobes associated with most targets. After the positive peaks are found as described for EM anomalies, the nearest point to the peak at amplitude zero or less is found and considered the zero-crossing point. Directions closer to the natural magnetic declination are favored. The picker proceeds past this point to the next local minimum on the same line, then finds the off-line minimum, which represents the negative peak. An inverted uphill-walk algorithm is used to delineate the negative lobe. It is not always possible to isolate negative magnetic lobes that overlap, but recently we have observed that the magnetic auto-picker works better if the negative lobes are selected first; i.e. the method described above is run in reverse. An example is shown in **Figure 10**. Both of the EM and magnetic auto-pickers contain additional special-case rules; for example, it is desirable not to separate very close EM peaks because some EM anomalies are double-peaked due to the survey-coil geometry; the distance criterion is selectable by the user.

6.2 MODEL DEVELOPMENT AND TESTING

6.2.1 Magnetic Modeling

Dipole Fits to an Ellipsoid Model

An analytic solution for the magnetic response of an arbitrarily oriented, triaxial ellipsoid in a uniform external field was derived and programmed. The model was compared in detail to the well-known response of a sphere (point dipole); in particular, the applicability of fitting spherical models to synthetic data for ellipsoids was tested and is reported in detail here. Preliminary progress on inversion for the parameters of an ellipsoid is also reported. A trial version of the ellipsoidal model has been incorporated into the developmental *MTADS* DAS; revisions will occur for joint inversion and model calibration.

The baseline *MTADS* DAS fits a dipole model to magnetic anomalies. In most cases this closely approximates the data, with goodness-of-fit parameter commonly of >99%. However, *MTADS* analysts observe that shallow or irregularly shaped objects gave lower goodness-of-fit, which suggested that there is additional information to be recovered beyond the dipole model.

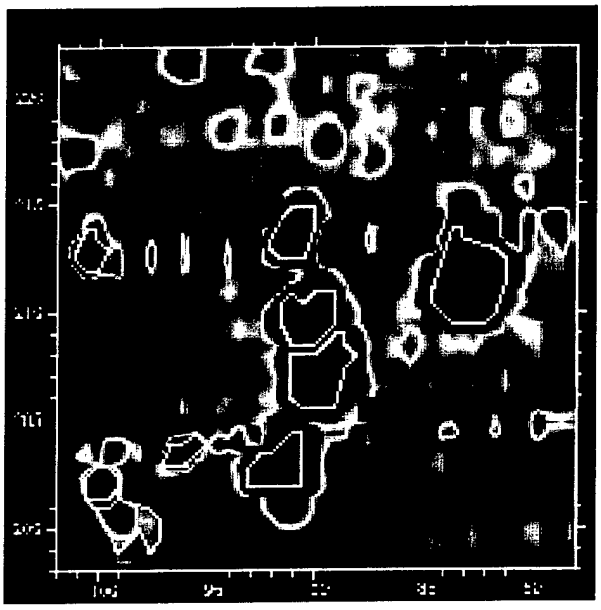

Figure 9. Autopicker results on Fig. 3 (threshold 5 mV, base fraction 0.1, minimum anomaly separation 1.2 m; see text for explanation). The autopicker is designed to trace individual anomaly shapes as best as possible, including closely spaced anomalies, in order to select spatially associated ungridded data for subsequent presentation to modeling and discrimination algorithms (note angular shape of bottom anomaly is due to a gridding artifact).

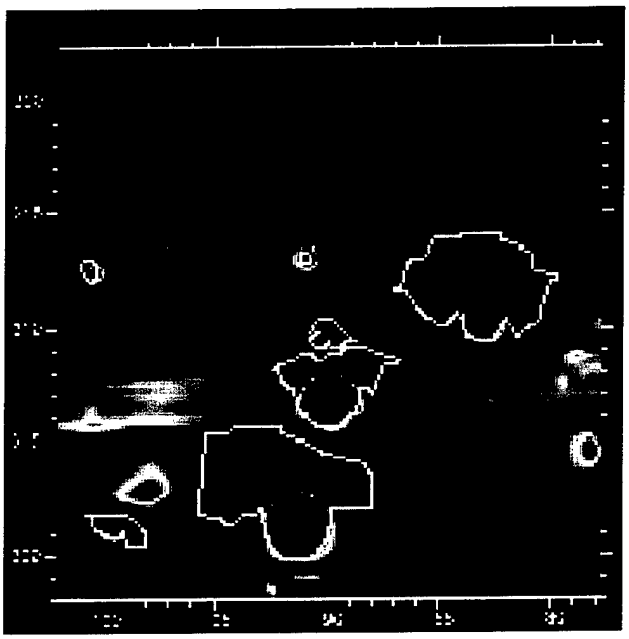

Figure 10. Autopicker results on magnetic image of same area as previous figure (threshold 20 nT, minimum signal 7 nT, minimum anomaly separation 1.2 m; see text for explanation). Magnetic autopicker must form dipoles by associating low with high anomalies.

Techniques to Create Synthetic Data

This hypothesis has been tested by generating synthetic data for ellipsoids and fitting the results to a dipole. Three simulated objects with approximately the same volume were tested: a 155mm projectile, a 2.75" rocket, and a piece of flat ferrous scrap. As a rule of thumb, the dipole fits are near-perfect when the object is distant by a few times its longest dimension ("in the far zone"), but degrade rapidly when the object is closer than its size ("the near zone"). Object depths are well estimated in the far zone by the dipole model. As the near zone is approached, depths are generally overestimated when targets are flat-lying and underestimated when inclined. Very shallow (~0.1 m) objects can have depths mis-estimated by a factor of two or more; this is of no practical consequence.

Object sizes tend to be overestimated by the dipole model. For typical ordnance, such as the 155mm projectile in the far zone, the estimated volume is about 30% greater than the size of a sphere with the same volume as the projectile. This factor is in good agreement with empirical "ordnance" corrections found by others. However, the (synthetic data) 2.75 in. rocket is overestimated by an average factor of 2.6 in the far zone, whereas the flat plate is overestimated by about 50%.

These results imply that there is significant additional shape information which can be recovered by inverting the ellipsoidal model for near-zone objects. Although dipole fits are typically excellent in the far zone, the estimated size still depends strongly on the dimensions of the target. Conversely, the quality of these far-zone fits also suggests inversion for ellipsoidal shapes will be under-determined using total-field magnetic data alone.

The ellipsoidal magnetic model computes both the vector-field and the total-field response of a triaxial ellipsoid in a uniform magnetic field at any point external to the ellipsoid (i.e., the finite size of the ellipsoid is considered). A sample input file to the model is:

```
1           # idipole: 1=> full form solution; 2=> dipole form solution
            0. 0. 0. # (xo,yo,zo) - object origin (meters)

2           # 1=> read (x,y,z) station locations from file, 2=>compute (x,y,z) internally

3.          # zval (plane of observation) (meters)
-4 0.2 41   # (xmin dx nx) on plane of observation (meters)
-4 0.2 41   # (ymin dy ny) on plane of observation (meters)
200 1       # target permeability  rel. to mu0 and background permeability
.035 .035 .7 # lengths of semi-major axes a b c (meters)
60000       # magnitude of background field (e.g. gammas, gauss, tesla)
8 73        # declination and dip of background field (deg)
90 45  0    # Euler angles (alpha beta gamma) of target in degrees
            #alpha = 90-N.azimuth, beta = 90-inclination,
            #gamma=not used for rotationally symmetric objects
```

Note that the two widely used orientation parameters azimuth and inclination are transformed to Euler angles .

The semimajor axes a, b, c of the ellipsoid define the target shape. Here three representative items were selected for analysis: A 155 mm projectile (a = b = 7.8 cm, c = 26.4 cm), a 2.75 in. rocket (a = b =3.5 cm, c = 70 cm), and a flat disc representative of scrap (a = b = 20 cm, c = 2 cm). The diameters of spheres with volumes equivalent to these objects are 23.4, 19.0, and 18.6 cm, respectively. The objects were modeled as functions of depth, inclination, and azimuth. The relative permeability was fixed at 200, characteristic of steel. The background noise field was taken to be approximately that of the Badlands Bombing Range, South Dakota, for which extensive *MTADS* data and ground truth will be used later to test these results.

We compute "data" from the ellipsoidal model and solve for the best-fitting dipole parameters. The dipole response is widely used to model UXO and has previously been incorporated into the baseline *MTADS*-DAS. The forward model for the induced dipole is:

$$B(r,q) = B_0 V[(\mu_r-1)/\mu_r](3\cos 2\theta-1)/r^3$$

where B_0 is the magnitude of the inducing field, V is the volume of the target, μ_r is the relative

magnetic permeability, r is the target-observation distance and θ is the angle between the target-observation vector $\underline{r}$ and the inducing magnetic field's unit vector $\underline{b}$. The latter may be determined from $\cos\theta = b \cdot r/r$.

The dipole-inversion algorithm was modified from forward and inverse implementation of the EM response of a sphere. The inversion begins with a number of iterations of an evolutionary programming algorithm to select a starting solution, then switches to the generalized-inverse gradient descent to determine the final solution. If a satisfactory solution is not found, the algorithm restarts evolutionary programming. When the model (dipole) fits are good, the algorithm requires only a dozen iterations or less. When the dipole is a poor fit to the ellipsoidal solution, numerous iterations and restarts can be required, which sometimes converge to incorrect solutions. All cases were tested by running the inversion at least 2-3 times to check for consistency.

Six parameters were allowed to vary freely for the dipole inversions: x,y,z location of the target, diameter of the fitted sphere, and inclination and declination of the inducing field. The magnitude of the inducing field was held constant at the reference value; note, however, that strong tradeoffs occur between the magnitude of the inducing field Ñor remnant magnetism Ñand the apparent size of the target. In other words, an object with strong remnant magnetism will appear to be larger than its true size.

The computational grids were varied to maintain dimensions greater than or equal to twice the object depth. The data spacing was varied commensurately from 0.05-0.2 m. There is a small (second significant figure) dependence of the inversion results on the gridding. With the fixed spacing of *MTADS* data, we expect strong variations in the solutions for very shallow objects as a function of the sampling.

The response of the 155mm projectile was studied in detail. Results for the ellipsoid and est-fitting dipole for a flat-lying projectile at 2-m depth are shown in **Figures 3a-3b.** As the projectile is rotated from azimuth 0° (**Figure 11**) to azimuth 45° (**Figure 12**), the magnetic-field orientation follows. However, as the projectile approaches azimuth 90° (**Figure 13**), the pattern "snaps back" to near the declination azimuth as the dominant polarization switches from longitudinal to transverse.

The magnetic field for a projectile that is inclined against the background field (inclination +45°) appears to be more monopolar and lower magnitude (**Figure 14**), because the induced field partially cancels the background field. Conversely, a projectile that is inclined towards the background field (-45°) produces a dipole that is much more pronounced than the reference case, due to the addition of the fields (**Figure 15**). The largest magnitudes are observed for vertical targets (**Figure 16**).

As the target depth is reduced, the field pattern changes markedly from that of a dipole (**Figure 17**). The quality of the dipole fit for the 155mm projectile degrades rapidly for targets shallower than 0.5 m (**Figure 18**).

This depth corresponds roughly to the length of the projectile. This behavior allows us to spatially separate the response for the ellipsoid into classical "near" and "far" zones. In the far zone, at observation distances greater than a few times the length of the object's long axis, the dipole fit is excellent. In the near zone, within a distance about equal to the object's size, the effects of ellipsoidal shape are strong, and the resulting field departs strongly that of a sphere or dipole.

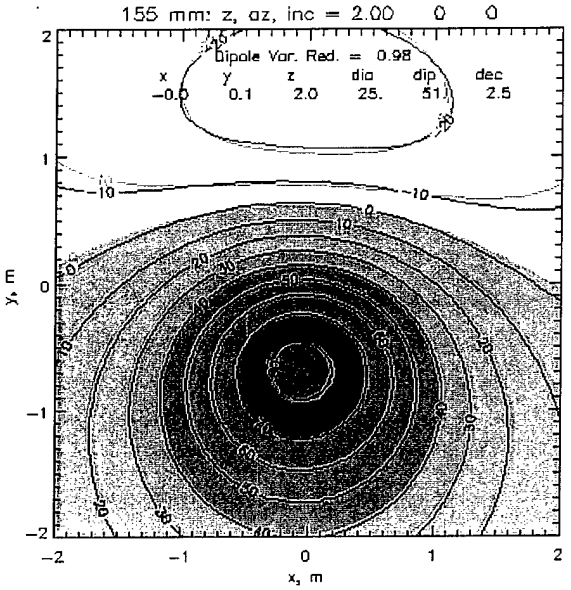

Figure 11. Field of simulated 155mm projectile (filled contours) compared to best-fitting dipole (open contours), for projectile depth 2 m, inclination 0, azimuth 0. 5.

Because the determination of the near and far zones depends on target size, the effects of an ellipsoidal shape is more pronounced at more extreme aspect ratios. The field of a simulated 2.75" rocket begins to be significantly misfit at depths less than about 1 m (**Figure 19**), which is consistent with this object's length nearly twice that of the 155mm projectile.

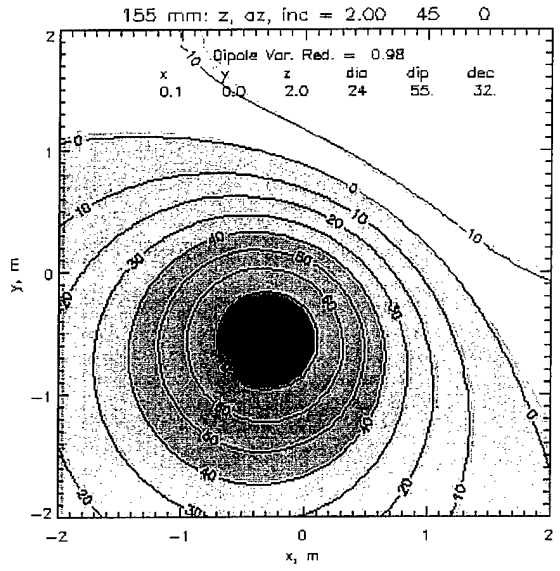

Figure 12. As Fig. 11, projectile inclination 0, azimuth 45.

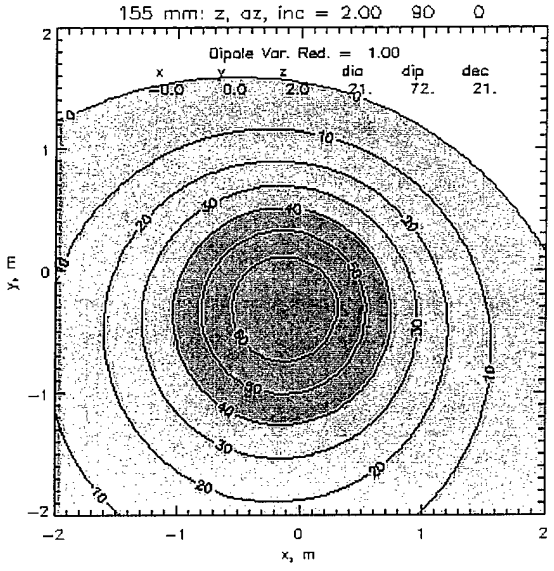

Figure 13. As Fig. 11, projectile inclination 0, azimuth 90.

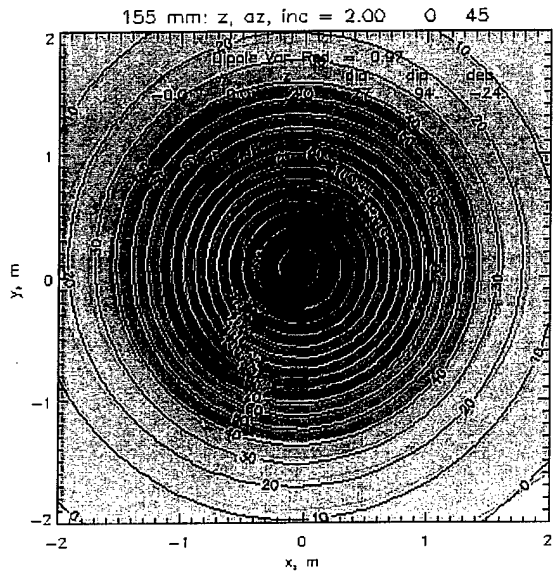

Figure 14. As Fig. 11, projectile inclination +45, azimuth 0.

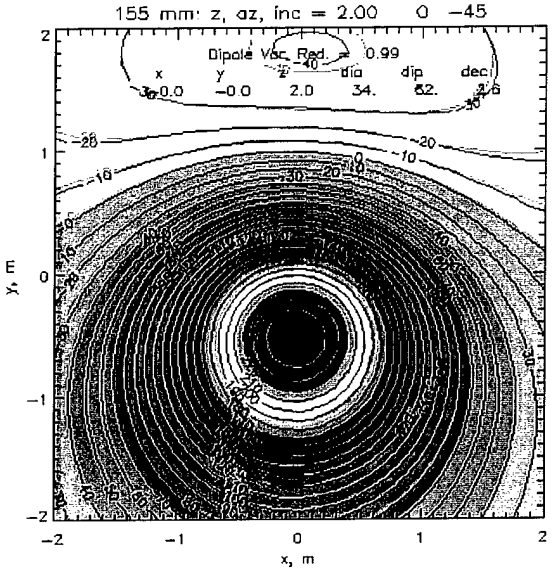

Figure 15. As shown in Fig. 11, projectile inclination -45, azimuth 0.

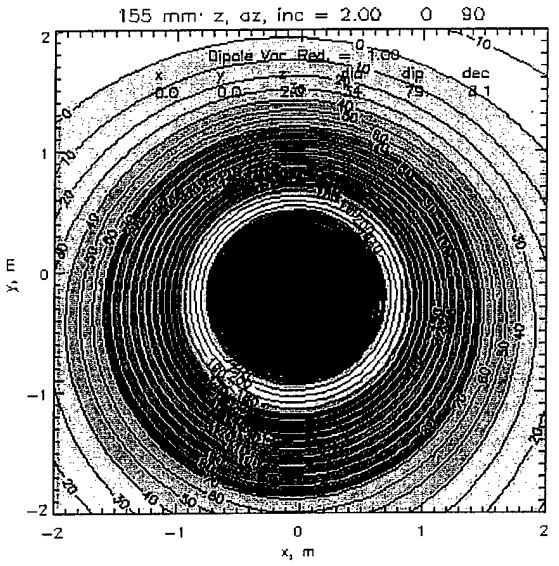

Figure 16. As Fig. 11, projectile inclination 90.

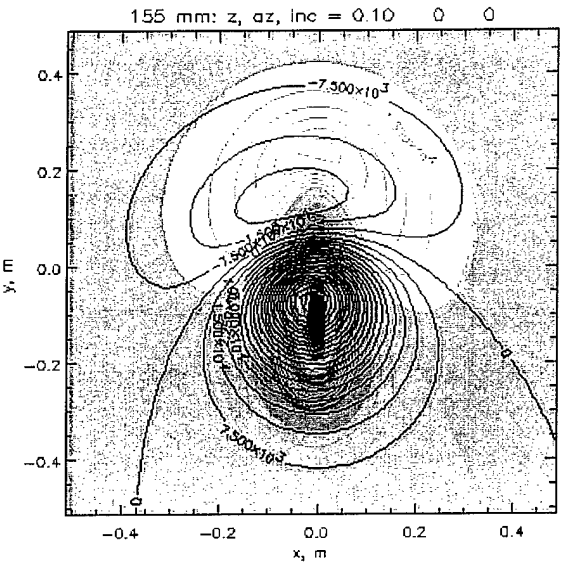

Figure 17. As shown in Fig. 11, projectile depth 0.1 m, inclination 0, azimuth 0.

Similarly, the 0.4-m wide simulated flat scrap departs from the dipole at about 0.5 m (**Figure 20**). Also note that the extreme aspect ratio of the rocket introduces greater scatter in the dipole fit due to target orientation. When targets lie in the far zone, the dipole model accurately estimates depths (**Figure 21**).

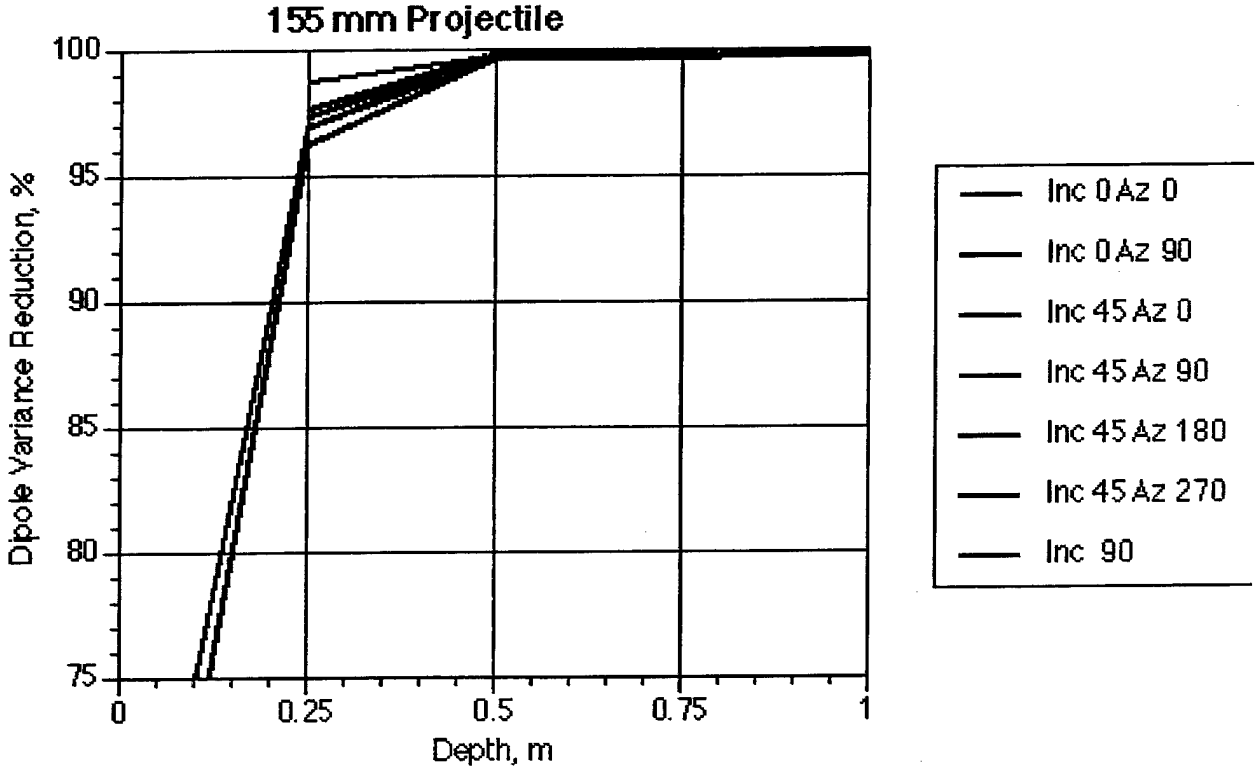

Figure 18. Quality of dipole fit for simulated 155mm projectile as functions of depth and orientation. Dependence on orientation is weak, but fits degrade rapidly for depths less than 0.5 m. Compare to projectile length 0.53 m.

In general the dipole model infers larger apparent diameters when flat-lying targets are oriented parallel to the background field and smaller apparent diameters when the such objects are transverse to the background field. The largest apparent sizes occur for steeply inclined objects, fully parallel to the incident field. These results follow straightforwardly from the polarizability of an elongated ferrous object.

The dipole-inferred volume of the 155mm projectile in the far zone averages about 30% larger than the true volume (**Figure 22**). This factor has a relatively small variation (92-147%) and, for this object, the estimated size actually becomes more accurate as the target depth is decreased. A correction factor of 1/1.3 is in good agreement with the "ordnance factor" derived by AETC and incorporated into the Geometrics' MagMapper and NRL's baseline *MTADS* software. However, this

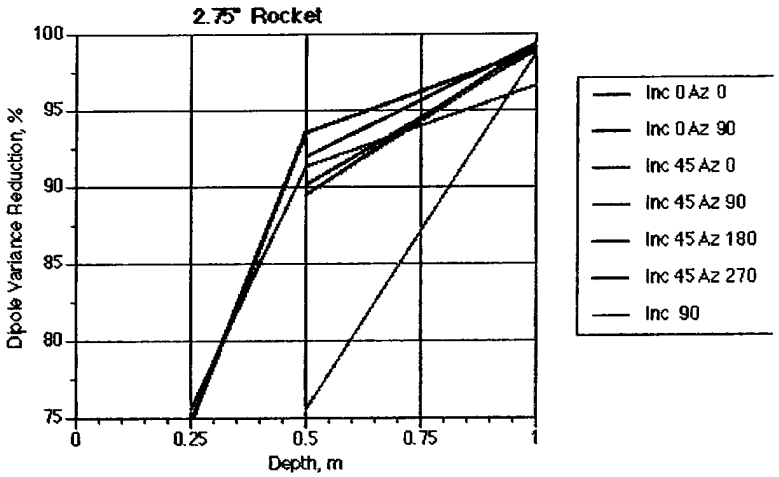

Figure 19. Quality of dipole fit for simulated 2.75" rocket. A larger scatter due to orientation is evident, and fits degrade rapidly for depths less than about 1 m. Compare to rocket length 0.7 m.

factor is not universal: in particular, the highly elongated rocket shows a wide scatter in apparent size which is more strongly controlled by orientation than by depth. Even at 3-m depth, the apparent size of the rocket varies by a factor of nearly 3 depending on orientation. The mean ratio of apparent to true volume appears to approach ~2.6. With the exception of very shallow depths, the flat scrap appears to be about 50% larger than its true size, with little variation. Nonetheless, these results show that both elongated and flattened objects tend to appear larger than their true size to the dipole model. This confirms the earlier qualitative prediction from the analytic formulation that far-zone effects of the ellipsoid's shape should be discernable.

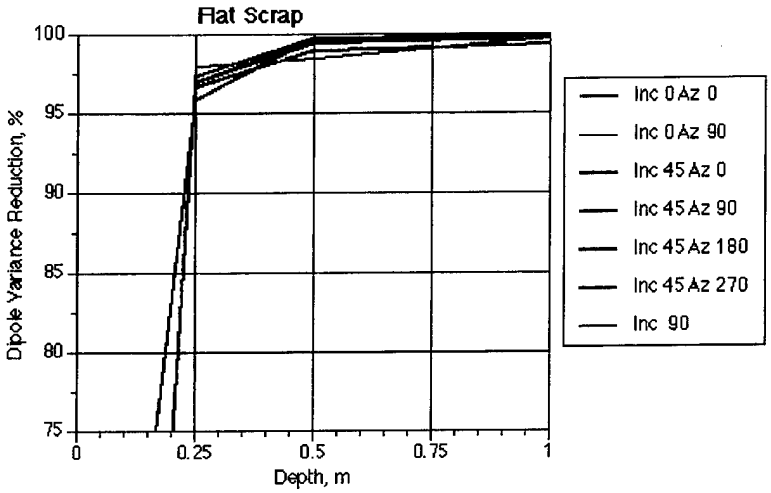

Figure 20. Quality of dipole fit for simulated flat scrap. Dependence on orientation is evident but intermediate between projectile and rocket. Fits degrade rapidly for depths less than about 0.5 m. Compare to scrap width 0.4 m.

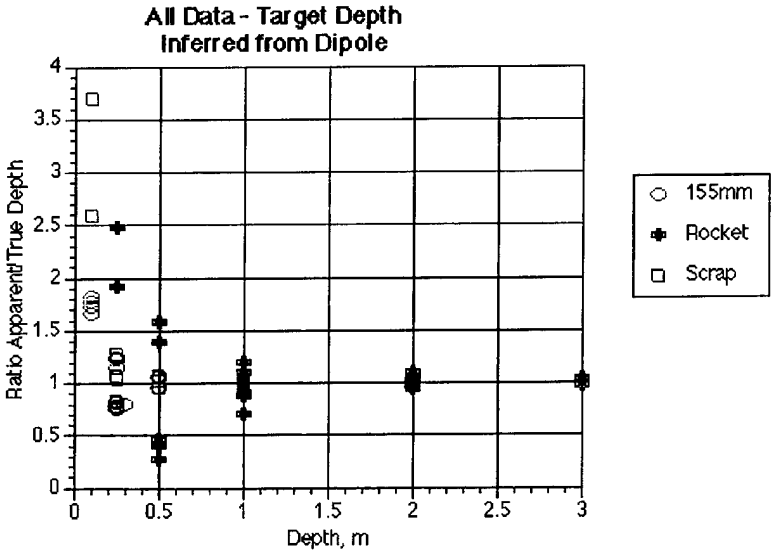

Figure 21. Apparent depth of objects derived from dipole model. Results are plotted for all orientations. Depths predicted from the dipole model are excellent for simulated UXO and OEW at distances from the sensor greater than 1 meter.

In summary, comparison of the induced-magnetic fields of the ellipsoid and the dipole (sphere) shows that the discrete shape of the ellipsoid becomes very evident in the near zone, or at observation distances less than about the object's longest dimension. In the far zone the field nearly perfectly matches that of a dipole and depth estimates are accurate, but sizes are variably overestimated by the dipole model; thus, the far-zone field still contains information on the the object's shape and orientation. These results indicate that inversion in the near zone for ellipsoid dimensions should be attainable, but, as all far-zone fields look like dipoles, inversion there will be strongly nonunique. Target volume, aspect ratio, and orientation will all trade off. Therefore, successful far-zone inversions using total-field magnetic data alone is doubtful, although tensor data and/or joint inversion with EM may provide additional constraints.

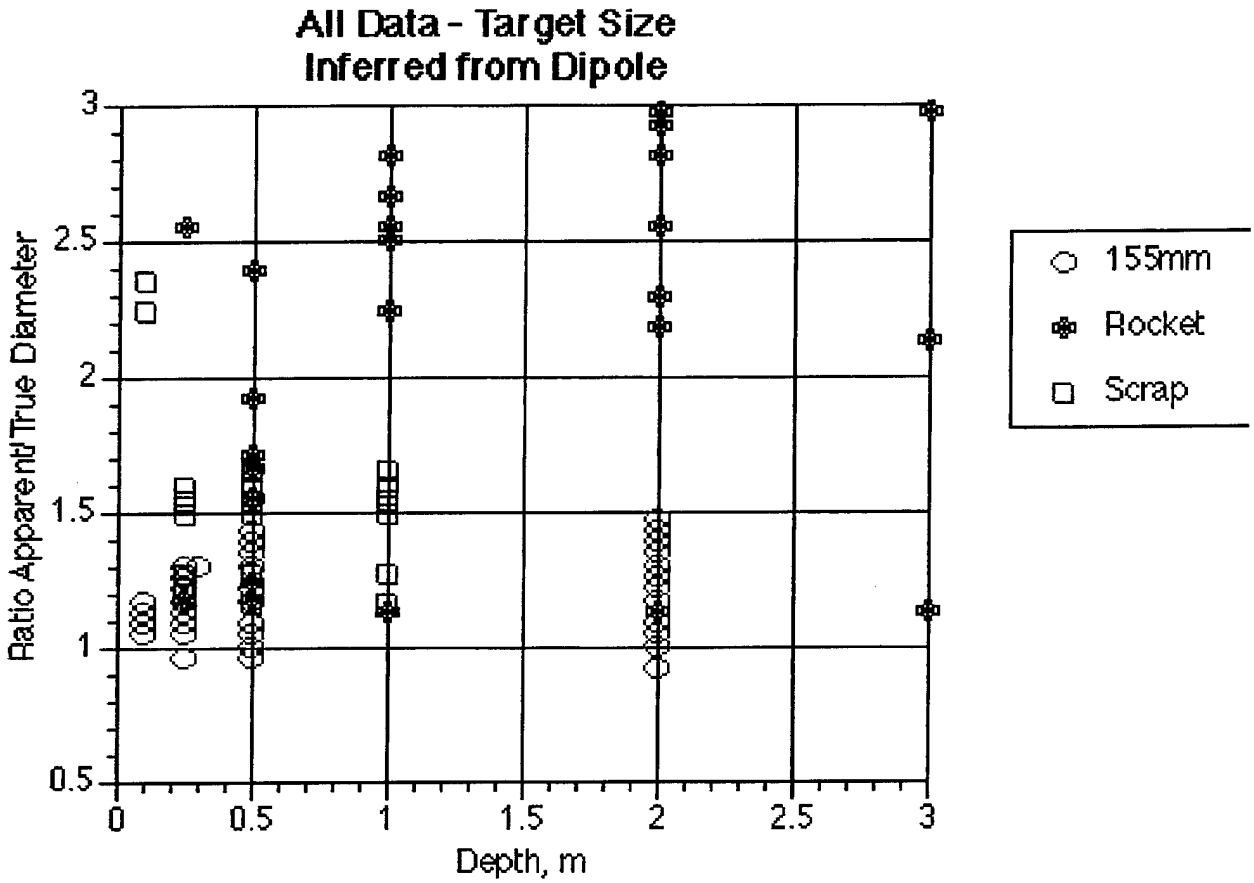

Figure 22. Apparent volume (diameter) of objects derived from dipole model. Results are plotted for all orientations. Object size inferred from the dipole model depend strongly on the target aspect ratio and orientation, even at great distances.

Inversion for Ellipsoid

The inverse problem has been fully implemented for the ellipsoid, in which the inferred parameters are :

1) diameter
2) aspect ratio
3) x-position
4) y-position
5) z-position (depth)
6) azimuth
7) inclination

We have assumed that targets are rotationally symmetric, so that only two shape and two orientation parameters are required. The azimuth and inclination are specified with respect to the target's symmetry axis. The target permeability is held fixed.

Preliminary tests were performed using the same synthetic objects described above, and the inversion code was able to recover all seven parameters accurately. However, a large number of iterations, including automatic restarts, were often required to find the part of the parameter space containing the correct solution. This follows directly from the results above: at sufficient distance from the sensor, all objects show a dipole response, but the strength and orientation of that dipole still depends on the target's shape and orientation. Therefore the inverse problem for these latter parameters becomes nonunique. It is unlikely that the true shape and orientation could be recovered for real targets in the far zone. Joint inversion with EM may improve this.

6.2.2 Electromagnetic Modeling

The electromagnetic-response model is based on the mean-field theory developed for this and other UXO/land-mine programs by P. Weichman. The basic assumption of the theory is that the electromagnetic field has fully penetrated the target so that the field may be described by a Taylor-series expansion about its mean value. The zero'th order is the DC or magnetic response, the first order is the characteristic late-time decay, and higher orders represent the early time responses. The theory has been explicitly evaluated for ellipsoids to second order, and higher orders will be determined iteratively. The numerical implementation of the EM model is being developed simultaneously with the magnetic model, as both share many geometrical factors relevant to the ellipsoid.

6.2.3 Prism *vs* Ellipsoid Models

The original proposal stated that three-dimensional modeling non-equant shapes (i.e., elongated or flattened) characterisic of UXO or EOW would be implemented using a rectangular prism model. This choice was based on the relative simplicity of the existing solution for the magnetic response of a rectangular prism and on preliminary evaluation in cartesian geometry of the extended Born approximation for electromagnetic induction. However, introduction of sharp corners makes the EM boundary conditions more complex, and we decided to evaluate mean-field EM theory in ellipsoidal coordinates in which these variations are smooth. Furthermore, objects with sharp corners require high-order modes to model the eddy currents there, which introduces substantially more computation time to get an accurate solution. As the zeroth-order EM theory is simply DC magnetic induction, evaluation of the mean-field theory through second order also provides the associated magnetic response for the ellipsoid.

We are still evaluating the differences in the responses of the ellipsoid and prism both in theory and in measurement. For magnetics, we are comparing the results of the complete analytic solutions of the ellipsoid and prism models, whereas for EM, we are examining the approximate time constants contributed by sharp corners. Field data are being acquired for a cube and a sphere, and for a square plate and a circular plate.

The present magnetic-field theory comparision between the two shapes is not fully consistent because the ellipsoid model includes demagnetization (the misalignment of internal and external fields due to internal self-cancellation), whereas the prism model allows the internal field to be specified independently, but does not explicitly compute the demagnetization. This difference is

maximized for flat objects perpendicular to the background field, which largely corresponds to the case of subhorizontal flat scrap (e.g., tail fins). Detailed comparison of such objects must await processing of field data for the flat plates and/or incorporation of demagnetization into the prism model.

Equant objects are not as strongly affected by demagnetization, so we compared the computed differences between a cube (200-cm width) and a sphere (248-cm width - equal volume to cube). MTADS magnetometer-acquisition parameters were used. At a depth of 0.25 m, the variances of the cube and the sphere were 99.89% identical. This fell to 87.7% with the target centroids at ground surface (**Figure 23**). Because of the differences in computed demagnetization, these values are upper bounds for edge and corner effects in observed magnetic fields for these test objects.

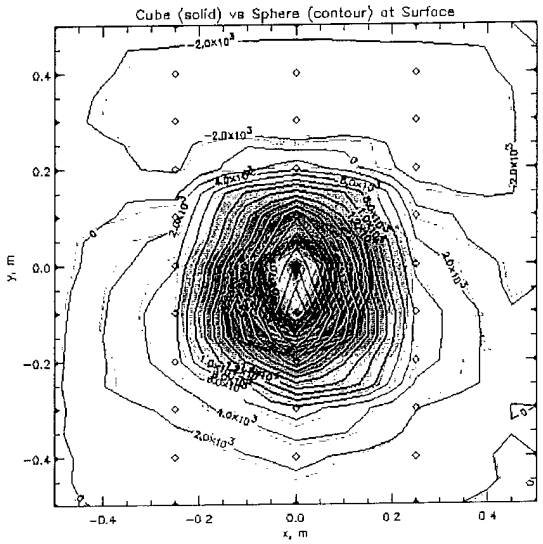

Figure 23. Computed MTADS magnetometer response for a 200-cm cube (filled contours) and an equal-volume sphere (open contours) with centroids at ground surface. Field variances are 87.7% identical.

Direct computation of the mean-field EM responses of prisms would require a substantial manpower investment that would noticeably detract from other project efforts. However, we can readily estimate the order-of-magnitude effect of sharp-cornered objects by considering the spatial scale of eddy currents required to map electrical flow in such corners (**Figure 24**). It is well-known that the eddy-current decay in any arbitrary solid can be described by a sum of exponentials (Kaufman, 1994), with the smaller, higher-order, time constants describing the current flow in more spatially restricted parts of the object. The first-order time constant is the decay that is preserved in "late time" and is commonly measured as "the" exponential decay.

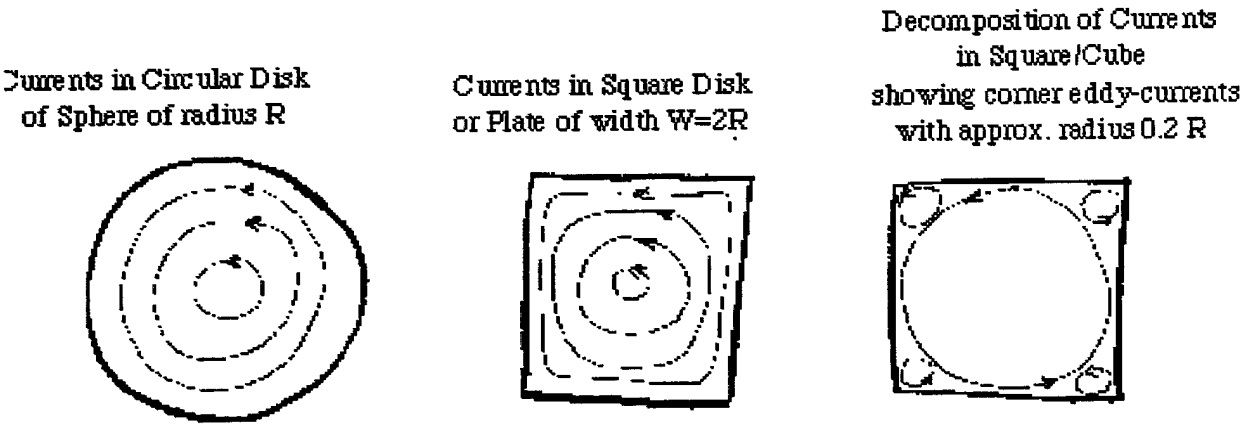

Figure 24. Schematic illustration of eddy currents in square and round plates or cubes and spheres. Currents required to fill corners have spatial scales about 20% of the largest current systems, and therefore decay faster than the characteristic late-time constant by a factor of 5 for plates and a factor of 25 for cubes.

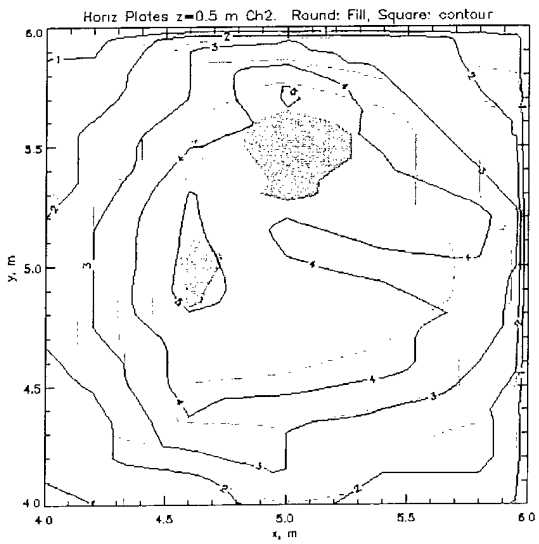

Figure 25. Observed EM-61 response for square plate (filled contours) and circular plate (open contours), with plate horizontal at 0.5-m depth. Field variances are 98% identical.

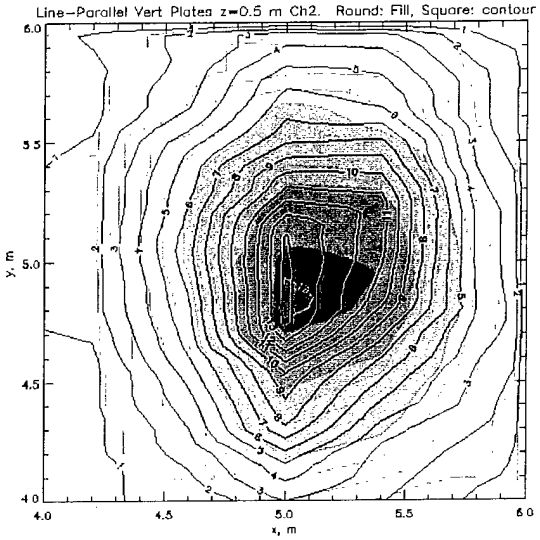

Figure 26. As Fig. 25, with plate vertical and oriented along-track (x-direction). Field variances are 96% identical.

Now the first-order time constant for a thin disk is t = msah/5.51 and that of a sphere is msa^2/p^2, where m is the permeability, s is the conductivity, a is the radius, and h is the thickness (Kaufman, 1994). These formulae also approximately apply to the decay times for the smaller current systems required for corner flow. As these areas have dimensions of order 20% of the first-order current system, it follows that the decay times for corner currents will be about 5 times faster in the square disk and 25 times faster in the cube than the late-time decay currents.

Flat non-ferrous scrap with width 10 cm and thickness 1 mm, representative of a tail fin, will have a first-order time constant of about 0.1 ms. The eddy currents associated with the corners will decay on time scales ~0.02 ms. This is much shorter than the MTADS time gate from 0.27-0.47 ms and therefore the difference between round and flat plates of this size cannot be detected by the *MTADS* EM system.

We compared the experimental measured EM response of two flat steel plates, one circular (17-cm diameter) and one square (15-cm diameter; both were 1.2 cm thick). The target centroids were 0.5 m deep and a standard EM-61 was used. The plates were oriented horizontally (**Figure 25**), vertically in the along-track direction (**Figure 26**), and vertically in the cross-track direction (**Figure 27**). The variance similarities between the two plates in these three tests were 98%, 96%, and 98%, respectively. The EM-61 time gate (0.42-0.82 ms) is of the same order of magnitude (tenths of a millisecond) as *MTADS*.

McNeill and Bosnar[14] measured the time-domain EM response for projectiles ranging from 80 to 155 mm caliber. They pointed out that the magnetic polarizability of these ferrous objects adds

will be of order tenths of a millisecond, which can be detected by *MTADS* given adequate data quality.

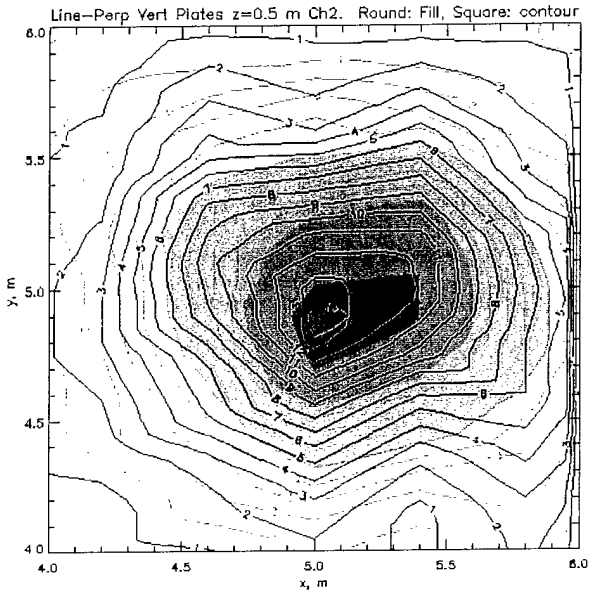

Figure 27. As Fig.25 with plate vertical and oriented across-track (y-direction). Field variances are 98% identical.

6.2.4 Joint Magnetic and EM Inversions

The joint inversion for mag and EM, as presently implemented, allows the user to select up to 14 independent parameters (target caliber and aspect ratio, xyz position, azimuth and inclination; background field strength, declination, and dip, target and background conductivity, target and background permeability). In practice, target and background conductivity and permeability are held constant, and the target orientation is specified by varying either its formal orientation parameters or the direction of the background field. Therefore 7 parameters are typical for inversion. The joint inversion uses the same techniques previously adopted, in which evolutionary programming (EP) defines the starting model and generalized-inverse (GI) gradient descent finalizes the solution. Alternatively, starting parameters can be read directly from a file or the *MTADS* interface and the EP step skipped. As the EP is relatively slow, we are experimenting with defining starting parameters from simple anomaly magnitude-width rules to improve the speed of solution convergence.

The essence of the joint inversion is the combination of both mag and EM into one data vector and allowing the inverse methods to operate on this joint vector. Each kind of data is normalized by its root-mean-square value, and the user selects a relative weight for the mag data knowing that the effective weight of the EM is 2 (one for each channel). Therefore, a weight of zero is equivalent to having no mag data, whereas an infinite mag weight will discount the EM data.

The EM model as presently implemented uses a quasi-empirical solution for the ellipsoid. This will be replaced by the mean-field theory within a few months. While the accuracy of this interim method is limited, it does allow for self-consistent simulations of joint inversion.

Preliminary numerical experiments demonstrate that the joint inversion is functioning correctly. However, in these tests on synthetic data there is often no significant improvement due to the joint inversion because the data from each sensor is well-fit in individual inversions. One improvement that was noted is that the EM helps the mag to converge in the "far zone" where the mag solutions are not unique (**Figure 28**).

6.2.4 Joint Magnetic and EM Inversions

The joint inversion for mag and EM, as presently implemented, allows the user to select up to 14 independent parameters (target caliber and aspect ratio, xyz position, azimuth and inclination; background field strength, declination, and dip, target and background conductivity, target and background permeability). In practice, target and background conductivity and permeability are held constant, and the target orientation is specified by varying either its formal orientation parameters or the direction of the background field. Therefore 7 parameters are typical for inversion. The joint inversion uses the same techniques previously adopted, in which evolutionary programming (EP) defines the starting model and generalized-inverse (GI) gradient descent finalizes the solution. Alternatively, starting parameters can be read directly from a file or the *MTADS* interface and the EP step skipped. As the EP is relatively slow, we are experimenting with defining starting parameters from simple anomaly magnitude-width rules to improve the speed of solution convergence.

The essence of the joint inversion is the combination of both mag and EM into one data vector and allowing the inverse methods to operate on this joint vector. Each kind of data is normalized by its root-mean-square value, and the user selects a relative weight for the mag data knowing that the effective weight of the EM is 2 (one for each channel). Therefore, a weight of zero is equivalent to having no mag data, whereas an infinite mag weight will discount the EM data.

The EM model as presently implemented uses a quasi-empirical solution for the ellipsoid. This will be replaced by the mean-field theory within a few months. While the accuracy of this interim method is limited, it does allow for self-consistent simulations of joint inversion.

Preliminary numerical experiments demonstrate that the joint inversion is functioning correctly. However, in these tests on synthetic data there is often no significant improvement due to the joint inversion because the data from each sensor is well-fit in individual inversions. One improvement that was noted is that the EM helps the mag to converge in the "far zone" where the mag solutions are not unique (**Figure 28**).

6.2.5 Model Calibrations

Model calibration consists both of comparing newly developed, complex models to existing, simple models and comparing models to data. The comparison of the magnetic response of the ellipsoid versus the sphere given in detail above validates the asymptotic behavior of the ellipsoid model as well as showing where the ellipsoid differs from the sphere. A similar analysis will soon be undertaken for the EM.

6.3 DEVELOPMENTAL DAS AND RELEASE NOTES

One of the final deliverables of the project CU-1092 is a new version of the *MTADS* DAS GUI that incorporates all the individual developmental components of this project. We have found it

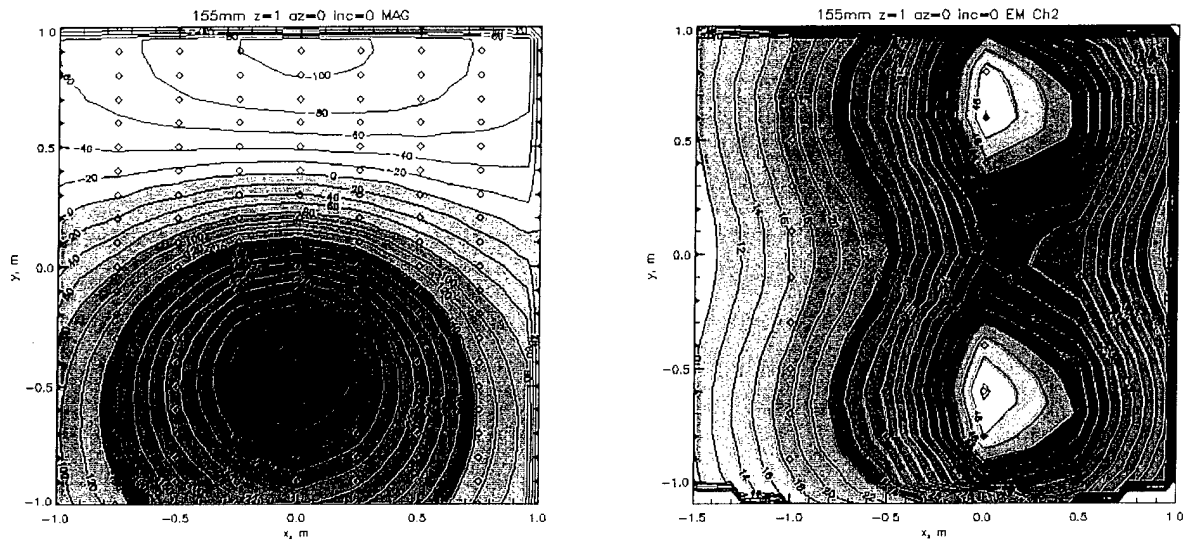

Figure 28. Results of joint inversions using ellipsoids for Mag (left and EM (right) for a simulated 155mm projectile.

expedient to begin this process earlier in the program to allow *in situ* testing of these new capabilities in the framework of the overall analysis process. There therefore currently exists a developmental version of the DAS GUI on SGI workstations both at Blackhawk and at NRL. Version control is being exercised and the two systems are being kept current by use of network connections. For the time being we have implemented and retain digital filter options including "Detrend," "Boxcar," Gaussian," "LoG," "Fourier," and "Wavelets." They are all available for study and evaluation using existing or new data sets. Eventually, less useful filters will be eliminated as options.

Developmental GUI Release Notes

The use of Release Notes with the developmental GUI provides documentation on new features or other changes made to the baseline *MTADS* DAS. They are available for researchers at both institutions as an aid to guide in evaluation of new capabilities. Below we show the release notes as they apply to the Internal Version 0.5.

The Project, Input, Auxiliary, and Report menus are unchanged. Submenus of the Input menu regarding survey processing have been changed to allow the selection of a grid pixel size for the interpolated survey image, and to allow the input of XYZ-formatted raw data.

The bulk of the changes in the *MTADS* DAS to date have occurred in the Analysis tool. One Analysis tool (i.e. window) functions for all data types (em, mag, ...). The fundamental unit of analysis is a "session." Each session is associated with one target list and one or two surveys for viewing on the dual screen. The Analysis menu contains buttons for New and Current sessions. A new session contains an empty target list and no surveys, while the current session refers to the

most recently used target list and surveys. Sessions can be saved and restored using the "Save" and "Restore" buttons in the Analysis tool.

Analysis Tool: The functions of the buttons are as follows:

Model One: Model a single selected anomaly. Currently under implementation.

Model All: Model all anomalies in target list. Currently under implementation.

Clear All: Clear all anomalies from target list.

Print: Print the target list. Not supported in version 0.2.

Save: Save this session under a user-defined name.

Restore: Restore a previously saved session.

Exit: Exit the Analysis Tool.

Define: Define the boundaries of an anomaly using the mouse.

Delete: Delete the selected anomaly.

Site View: View the entire site for surveys shown.

Overlay: As in original MTADS version, select objects to overlay on the interpolated image.

PCA: Perform a PCA analysis of up to three images. Further information on PCA analysis is given below.

UTM, Shift width, XY Axes, arrow: as in original MTADS.

The following buttons are specific to each of the two drawing windows and the associated survey for that window:

Survey menu: Select a survey for this draw window.

Image menu: Select an image for this draw window, generally either a gridded image of the raw data, a pixel view of the raw data, or a filtered or PCA image.

Filter: Perform a filter operation on any image within this survey.

Output: Perform PostScript or other output; these functions are not fully tested in this version.

Auto Pick: Automatically select anomalies. Further information on automatic picking is provided below.

Settings: For pixel views only, define the pixel size.

Annotate: Add annotations such as arrows, text, circles to the image.

The functions of the buttons on the automatic anomaly picking menu are as follows:

Mag

Threshold: The lowest value for which an anomaly or anomaly group will be selected.

Base Type radio button: Use either absolute or fraction-of-peak basis for determining outside boundary of anomalies.

Base Value: For absolute base type, after a peak is selected by exceeding "Threshold", define the outside of the anomaly at a contour of this value.

Base Fraction: For fractional base type, after a peak is selected by exceeding "Threshold", define the outside of the anomaly at a contour of this fraction of the peak value.

Proximity Threshold: A dimensionless values indicating how far to reach to associate a positive anomaly with a negative anomaly. A lower number cause the auto-picker to reach farther to make associations; a higher number requires positives to be closer to negatives.

Minimum Separation Distance: Anomalies separated by less than this distance are considered one anomaly.

Magnetic Declination: Specify the declination at the survey site.

Search Area (Entire Site or Current Window): Specify the area over which to run the automatic anomaly picker.

EM

Threshold: The lowest value for which an anomaly or anomaly group will be selected.

Base Type radio button: Use either absolute or fraction-of-peak basis for determining outside boundary of anomalies.

Base Value: For absolute base type, after a peak is selected by exceeding "Threshold", define the outside of the anomaly at a contour of this value.

Base Fraction: For fractional base type, after a peak is selected by exceeding "Threshold",

define the outside of the anomaly at a contour of this fraction of the peak value.

Minimum Separation Distance: Anomalies separated by less than this distance are considered one anomaly.

Search Area (Entire Site or Current Window): Specify the area over which to run the automatic anomaly picker.

To perform PCA analysis, two or three images are selected in the PCA Tool dialog box. PCA operations can be performed sequentially, so it is possible to combine two images and then combine a third image with the first result. For example, upper and lower coil EM61 images may be merged via PCA and then subsequently combined with a mag image. Since the inputs to a PCA may be from different surveys, the result is not considered a new image in one of the input surveys; rather, it is considered a new survey in and of itself. Look for the new PCA image name on the survey menu under either draw window.

7. REFERENCES

1. H.H Nelson, J.R. McDonald, and R. Robertson, "*MTADS* TECHEVAL Demonstration," NRL/PU/6110-97-348, October 1996.
2. "Unexploded Ordnance Advanced Technology Demonstration Program at Jefferson Proving Ground (Phase I)," U.S. Army Environmental Center, Report No. SFIM-AEC-ET-CR-94120, December 1994.
3. "Evaluation of Individual Demonstrator Performance at the Unexploded ordnance Advanced Technology Demonstration Program at Jefferson Proving Ground (Phase I)," U.S. Army Environmental Center, Report No. SFIM-AEC-ET-CR-95033, March 1995.
4. "Unexploded Ordnance Advanced Technology Demonstration Program at Jefferson Proving Ground (Phase II)," U.S. Army Environmental Center, Report No. SFIM-AEC-ET-CR-96170, June 1996.
5. J.R. McDonald, H.H. Nelson, and R. Robertson, "Results of the MTADS Technology Demonstration #2 at the Magnetic Test Range", Marine Corps Air Ground Combat Center (MCAGCC), Twentynine Palms, CA, NRL/PU/6110-97-349, December 1996.
6. J.R. McDonald, H.H. Nelson, J. Neese, R. Robertson and R.A. Jeffries, "MTADS Unexploded Ordnance Operations at the Badlands Bombing Range," Pine Ridge Reservation, Cuny Table, S.D., NRL/PU/6110-98-353, July 1997.
7. "MATLAB Image Processing Toolbox User's Guide", Mathworks, Inc., Natick, MA, 1997.
8. "IDL Reference Guide", Research Systems, Inc., Boulder, CO, IDL Version 5.0, March , 1997.
9. W.H. Press, S.A. Teukolsky, W.T. Vetterling, B.P. Flannery, *Numerical Recipes in C: the Art of Scientific Computing*, Cambridge University Press, Cambridge, UK, 1992.
10. K. Esbensen and P. Geladi, "Strategy of Multivariate Image Analysis," *Chemometrics and Intelligent Laboratory Systems*, **7**, 1989, 67-86.
11. R. Bro, "Multiway Calibration. Multilinear PLS," *J. Chemometrics*, **10,** 1996, 47.
12. R.E. Shaffer, S.L. Rose-Pehrsson, and R.A. McGill, "Multiway Analysis of Preconcentrator-Sampled Surface Acoustic Wave Chemical Sensor Array Data," *Field Analytical Chemistry and Technology*, **2**, 1998, 179-192.
13. Kaufmann, A.A., "Geophysical Field Theory and Methods, Part C," Academic Press. San Diego. 1994, p. 335
14. J.D. McNeill,, and M,. Bosnar, "Applications of Time Domain Electromagnetic Techniques to UXO Detection," UXO FORUM 1996, pp. 34-42

APPENDIX OF PUBLICATIONS

PEER REVIEWED JOURNAL ARTICLES AND/OR PAPERS

None.

TECHNICAL REPORTS

Memorandum Report Ser. 6110/330 of 19 November 1998. "Summary of Second Quarterly Review for SERDP Program CU-1092."

CONFERENCE/SYMPOSIA PROCEEDINGS

"UXO Target Detection Using Magnetometry and EM Survey Data," Susan Rose-Pehrsson, R. E. Shaffer, J.R. McDonald, H.H. Nelson, R.E. Grimm and T.A. Sprout, SPIE International Symposium on Industrial and Environmental Monitors and Biosensors, Bosaton, MA, 2 November 1998.

"UXO Site Characterization and Remediation Using the MTADS Technology," J.R. McDonald, The 3rd Annual SERDP Symposium and Workshop, Arlington, VA, 1 December 1998

"Joint Magnetic and EM Discrimination of UXO Using MTADS," Bob Grimm, The 3rd Annual SERDP Symposium and Workshop, Arlington, VA, 1 December 1998

PUBLISHED TECHNICAL ABSTRACTS

None.

PUBLISHED TEXT BOOKS OR BOOK CHAPTERS

None.